Published in final edited form as:
Cancer Res. 2010 February 15; 70(4): 1555. doi:10.1158/0008-5472.CAN-09-3067.

Liver-Directed Irreversible Electroporation Therapy: Longitudinal Efficacy Studies in a Rat Model of Hepatocellular Carcinoma

Yang Guo, MD[1], **Yue Zhang, BS**[1,2], **Rachel Klein, BS**[1], **Grace M. Nijm, Ph.D.**[3], **Alan V. Sahakian, Ph.D.**[3], **Reed A. Omary, MD, MS**[1,4,5], **Guang-Yu Yang, MD, PhD**[4,6], and **Andrew C. Larson, PhD**[1,2,3,4,5]

Yang Guo: y-guo@northwestern.edu; Yue Zhang: yzhang52@uic.edu; Rachel Klein: r-klein@northwestern.edu; Grace M. Nijm: gracenijm2008@u.northwestern.edu; Alan V. Sahakian: sahakian@delta.ece.northwestern.edu; Reed A. Omary: reed@northwestern.edu; Guang-Yu Yang: g-yang@northwestern.edu; Andrew C. Larson: a-larson@northwestern.edu

[1]Department of Radiology, Northwestern University, Chicago, IL, USA

[2]Department of Bioengineering, University of Illinois at Chicago, Chicago, IL, USA

[3]Department of Electrical Engineering and Computer Science, Evanston, IL, USA

[4]Robert H. Lurie Comprehensive Cancer Center, Chicago, IL, USA

[5]Department of Biomedical Engineering, Northwestern University, Chicago, IL, USA

[6]Department of Pathology, Northwestern University, Chicago, IL, USA

Abstract

Irreversible electroporation (IRE) is an innovative local-regional therapy that involves delivery of intense electrical pulses to induce nano-scale cell membrane defects for tissue ablation. The purpose of this study was to investigate the feasibility of using irreversible electroporation as a liver-directed ablation technique for the treatment of hepatocellular carcinoma (HCC) in the N1-S1 rodent model. N1-S1 rat hepatoma was grown in 30 Sprague-Dawley rats; these animals were divided into treatment and control groups. For treatment groups, IRE electrodes were inserted and 8 100 μs 2500V pulses applied to ablate the targeted tumor tissues. For both treatment and control groups (6 rats/group), MRI scans were performed at base-line and 15-day follow-up intervals to measure tumor sizes (1D maximum diameter, Dmax, and estimated 2D cross-sectional area, Cmax) to determine longitudinal outcomes based upon observed size changes. Additional groups of treated animals were sacrificed at 1, 3, and 7-day intervals post-therapy for pathology assessment of treatment response. MR images demonstrated significant tumor size reductions within 15 days post-therapy (32±31% Dmax and 52 ±39% Cmax decreases compared to 110±35% Dmax and 286±125% Cmax increases for untreated tumors). Pathology correlation studies showed a clear progression from poorly differentiated viable

Contact information: Andrew C. Larson, Ph.D., Departments of Radiology and Biomedical Engineering, Northwestern University Feinberg School of Medicine, 737 N. Michigan Ave, 16th Floor, Chicago, IL 60611, phone: (312)926-3499 fax: (312)926-5991, a-larson@northwestern.edu.

Author Involvement:

Yang Guo: study concept and design, acquisition of data, statistical analyses, analysis and interpretation of data, drafting of manuscript
Yue Zhang: FEM simulation, acquisition of data, analysis and interpretation of data, critical revision of the manuscript for important intellectual content
Rachel Klein: acquisition of data
Grace M. Nijm: FEM simulation, revision of the manuscript for important intellectual content
Alan V. Sahakian: critical revision of the manuscript for important intellectual content
Reed A. Omary: critical revision of the manuscript for important intellectual content
Guang-Yu Yang: study concept and design, critical revision of the manuscript for important intellectual content
Andrew C. Larson: study concept and design, acquisition of data, statistical analyses, analysis and interpretation of data, critical revision of the manuscript for important intellectual content, study supervision

HCC tissues pre-therapy to extensive tumor necrosis and complete regression in 9 out of 10 treated rats 7–15 days after treatment. Our findings suggest that IRE was effective for targeted ablation of liver tumors in the N1-S1 rodent model; IRE may offer a promising new approach for liver-directed treatment of HCC.

Keywords

Liver ablation; therapy response; MRI; pathological evaluation; FEM simulation

Introduction

Hepatocellular carcinoma (HCC) is the sixth most common cancer worldwide and the third most common cause of cancer death (1,2). Resection, liver transplantation and percutaneous ablation treatments are three potentially curative therapies for early stage HCC; effective utilization of these therapies is increasing as a result of widely implemented surveillance programs in at risk patient populations (3). However, most patients are not candidates for resection or transplantation due to advanced disease stages and/or donor shortages (4).

According to the guidelines of the American Association for the Study of Liver Diseases (AASLD), percutaneous ablation is the best treatment option for nonsurgical patients with early stage HCC (5). These ablation techniques include percutaneous ethanol injection (PEI) (6), percutaneous acetic acid injection (PAI) (7), radiofrequency ablation (RFA) (8,9), microwave coagulation therapy (MCT) (10), laser interstitial thermal ablation (11) and cryoablation therapy (12). PEI is the most well known and widely studied approach; PEI can offer a safe, effective and inexpensive treatment for small HCC achieving tumor necrosis rates of 90–100% for HCC smaller than 2 cm. However, for HCC between 3 and 5 cm, this rate drops to 50% (13) and the local tumor recurrence rate is up to 17% when treating HCC $\geq$ 5 cm (14). RFA is the most widely used thermo-ablation technique providing improved local disease control compared with PEI in both small and larger HCC (5,15). However, RFA has significant potential limitations, including local tumor progression and a higher rate of adverse events (intra-peritoneal bleeding, tumor seeding, hepatic abscess, bile duct injury and hepatic decompensation) (16–18). Furthermore, depending upon the location of the targeted tumor, RFA may be contraindicated due to the potential damage to adjacent tissues and blood vessels (19). Therefore, the development of a more effective HCC ablation technique is warranted to achieve superior tumor necrosis rates while reducing the likelihood of adverse events.

Irreversible electroporation (IRE) is an innovative loco-regional therapy that was first introduced as a potential tissue ablation technique in 2005 (20). IRE involves targeted delivery of short (micro- to milli-second duration) intense electrical pulses to induce cell death through permanent cell membrane defects. These pulses elevate the trans-membrane potential to an extent that causes permanent defects within the lipid bi-layer of the cell membrane for those tissues contained with the targeted treatment region. These pulses are applied via electrodes positioned within the targeted tissues. Previous animal model studies have demonstrated that IRE can ablate substantial volumes of tissue. IRE has the potential to serve as an independent, new modality for targeted tissue ablation that is based upon the application of strong electrical fields rather than the deposition of heat or chemical agents (21–23). Rigorous pre-clinical studies in human hepatocellular carcinoma cells (HepG2) (24), normal liver (25) and prostate tissues (26), as well as cutaneous tumor models (22) have each demonstrated the feasibility of using IRE as a new ablation option with negligible thermal side-effects (27).

The purpose of our current study was to investigate the efficacy of IRE approaches for targeted ablation of HCC. We tested the hypothesis that IRE procedures would lead to tumor necrosis

in a transplanted rodent hepatoma model. We provide serial magnetic resonance imaging (MRI) and follow-up histopathological evidence demonstrating the potential longitudinal efficacy of IRE for the treatment of HCC.

Materials and Methods

Tumor Cell Line and Culture

The N1-S1 rat hepatoma cell line (ATCC, CRL-1603, Manassas, VA, USA) was obtained and cultured in Dulbecco's Modified Eagle's Medium (DMEM, ATCC, Manassas, VA, USA) supplemented with 10% fetal bovine serum (Sigma-Aldrich, MO, USA) and 90μg/ml gentamycin. Cells were maintained in suspension culture flasks at 37°C in a humidified atmosphere containing 5% CO2. This cell line was initially established from a hepatocellular carcinoma induced in a male Sprague–Dawley rat by ingestion of carcinogen 4-dimethylaminoazobenzene (28). Before each implantation procedure, the viability of the cells was tested with Trypan blue staining (confirming > 90% cell viability for each tumor implantation procedure).

Animal Model

All studies were approved by our institutional animal care and use committee and were performed in accordance with institutional guidelines. Forty-four adult male Sprague Dawley rats (Charles River Laboratories, Wilmington, MA, USA) weighting initially 301–325g were used for these experiments. After anesthesia, a mini-laporatomy was performed and the left medial lobe of the liver was exposed. 1×10^6 N1-S1 rat hepatoma cells were visually injected under the hepatic capsule into this lobe. Following initial implantation, approximately 6 to 10 days were required for tumor induction and growth to desired pre-treatment size (diameter < 1.60cm). 30 rats from the initial 44 implanted animals produced hepatoma (1.29 ± 0.18cm diameter) suitable for subsequent IRE treatment procedures. These rats were randomly divided into 6 groups, (Group 1) 6 rats for a non-treated baseline control group, (Group 2) 6 rats for a non-treated 15-day end point control group, (Group 3) 6 rats for an IRE-treated 15-day end point group, and 4 rats each for IRE-treated 1-day (Group 4), 3-day (Group 5), and 7-day (Group 6) end point groups. IRE procedures were performed shortly after baseline MRI measurements; these MRI measurements were repeated at baseline and 15-day follow-up time intervals to measure tumor sizes (group 2 and 3) with animals subsequently euthanized for histology at different study end points for each group (1, 3, 7, or 15 days intervals after original baseline scan).

Irreversible Electroporation (IRE) Procedures

IRE apparatus and dosing plan—A BTX Electroporator (ECM830; Harvard apparatus, Holliston, MA) function generator and a parallel two-needle electrode array were used for all rat IRE procedures. The electrode array was constructed using two MR compatible platinum-15% iridium needles (each 35mm in length with a diameter of 4mm); these were inserted through a plastic block to maintain a 1cm spacing between the two parallel needles. We elected to use an IRE ablation protocol that included the application of 2500V square wave pulses, a total of 8 pulses of 100μs length with 100ms spacing between pulses (identical to protocol used for prior IRE studies in cutaneous tumor tissues (22)). Prior to *in vivo* IRE procedures, we used a commercial finite element modeling (FEM) software package (COMSOL Multi-Physics, Version 3.3) to simulate the anticipated ablation zone based upon the above described IRE protocol parameters, electrode spacing, and anticipated lethal electrical field potential for hepatic tissues of 637 V/cm (29). Our simulation closely followed those described in previous IRE studies solving the Laplace equation to calculate induced electrical field potentials based upon anticipated tissue and electrode conductivities (20,30). Based upon our chosen IRE parameters, the FEM simulations suggested that we should

anticipate ablation zones of roughly 1.6cm×1.2cm (Fig. 1b), sufficiently large for treatment of the induced N1-S1 tumors. Also, use of a short time duration for application of the electrical pulses should lead to negligible heating effects (relatively short 100μs integration interval for Arhennius relation describing anticipated thermal damage $\Omega = \int \xi\, e^{-E/Rt}\, dt$, with frequency factor ξ, E activation energy and R universal gas constant (20,27)).

Tumor IRE procedure—Prior to both imaging and IRE procedures, rats were anesthetized with a high limb injection of Ketamine (75–100 mg/kg) and Xylazine (2–6 mg/kg). After baseline imaging for tumor confirmation, each rat was fixed in a supine position within a restrain apparatus (rats strapped to form-fitting back board). Next, a mini-laparotomy incision was performed to expose and visually locate the N1-S1 tumor within the left hepatic lobe. Prior to electrode placement, the tumor-bearing liver lobe was digitally palpated between thumb and forefinger to approximate the configuration of the tumor mass. For each animal, we positioned the bi-polar IRE electrode array such that the two needle insertion positions a) essentially straddled the centroid of the tumor mass and b) were aligned along the axis of the largest tumor dimension (for optimal treatment tumor should be located midway between the two parallel electrodes, Fig. 1). Finally, the electrodes were connected to the electroporation function generator and IRE pulse train applied (requiring <1s for application of the complete IRE pulse train). Following IRE procedure, the abdominal incisions were closed with 2-layer technique followed by topical application of antibiotic ointment and Metacam injection (1–2mg/kg SQ). Animals were returned to storage facilities for the duration of the follow-up delay interval prior to end point imaging studies. During these follow-up delay intervals, each animal was observed daily to determine the presence of any post-operative complications (incision infection or abscess formation); at necropsy each animal was inspected for additional procedural complications including injuries to adjacent organs, tumor seeding, and intra-peritoneal bleeding.

MRI Measurements

MRI protocol—All MRI studies were performed using a 3T Magnetom Trio clinical scanner (Siemens Medical Solutions, Erlangen, Germany) with custom-built rodent receiver coil (Chenguang Med. Tech. Co., Shanghai, China). Along both coronal and transverse orientations, T2-weighted, T1-weighted, and proton-density weighted turbo spin echo (TSE) scans were performed with a multi-slice acquisition providing complete coverage of the entire liver volume (31). All scans were performed with a 150mm FOV, 2.0mm slice-thickness, 3 signal averages, 256 matrix (0.6×0.6 mm^2 in-plane voxel size), repetition and echo time (TR/TE) = 3500/60ms for T2-weighted scans, TR/TE = 300/8ms for T1-weighted scan, and TR/TE = 3500/8ms for proton-density weighted scan. These MRI measurements were performed at baseline and at the end point of the study for each respective animal.

Image Analysis—Measurements were performed offline using the ImageJ software package (http://rsb.info.nih.gov/ij/). All coronal and axial orientation DICOM format T2W TSE images collected for each animal were reviewed according to RECIST and WHO criteria to a) measure the maximum lesion diameter (D_{max}, along the orientation bearing the largest tumor diameter) (32) and b) provide an estimate of the 2D cross-sectional area of the tumors at these same locations (C_{max}, calculated as the cross-product of the maximum lesion diameter D_{max} and largest diameter measured perpendicular to D_{max}) (33). These measurements were performed for both baseline and 15-day follow-up interval scans.

Histology

After follow-up MRI measurements, each rat was euthanized with intravenous injection of Euthasol at a dose of 150 mg/kg and bilateral thoracotomy. 2–3 sections across the lesion were sampled and fixed in 10% formaldehyde solution; these tissue sections were then embedded

in paraffin for hematoxylin and eosin staining. Resulting histology slides were de-identified (w.r.t. treatment group) and reviewed by an attending surgical pathologist with specialization in gastrointestinal oncology (>10 years experience). The percentage of viable tumor tissue was separately evaluated for each animal.

Representative tissue sections from each group were selected for immunohistochemistry evaluation. CD34 staining was used as a malignant tumor neovascularization marker (34,35) to highlight regions of sinusoidal capillarization; caspase 3 staining (previously demonstrated during induction of hepatocyte apoptosis both in vitro and in vivo) was used as a marker of active apoptosis (36,37).

Statistical Analysis

All statistics were performed using the SPSS statistical software package (SPSS, version 17, Chicago, IL, USA). Lesion size increases based upon 1D D_{max} measurements and 2D C_{max} measurements were compared between Group 2 and Group 3 animals (comparison between untreated and treated rats after 15-day follow-up interval) by non-parametric Mann-Whitney U test. Test was considered statistically significant with a p-value < 0.05.

Results

32 of 44 rats implanted with N1-S1 cells developed hepatoma (73% tumor induction rate similar to previously reported N1-S1 induction rates ((38))). One rat was euthanized prior to IRE procedures due to suture failure and wound dehiscence and one additional rat excluded from the study due to excessive tumor growth prior to IRE procedure (detected during baseline MRI scan). No post-operative complications were observed in the IRE-treated rats (Groups 3–6).

H&E staining

The ablation zones anticipated based upon our FEM simulations were well correlated to *in vivo* IRE ablation zones observed within hematoxylin and eosin (H&E) pathology slides post-necropsy (Fig. 1c). Within tumor animals, H&E staining showed a clear progression from poorly differentiated viable hepatoma tissue pre-therapy, to heterogeneously viable tumor tissues early post-IRE (1–3 days) and extensive tumor necrosis at delayed intervals (7–15 days) post-IRE treatment (Fig. 2). A 95% viable hepatoma is shown from a representative baseline control animal in Fig. 2a. 1-day post-IRE, ablation zones showed mostly viable tumor and adjacent necrotizing liver tissue (Fig. 2b). 3-day post-IRE, ablation zones included both heterogeneously necrotizing tumor and liver tissues (Fig. 2c). In the 7-day post-IRE treatment animals (Group 6), 4 out of 4 treated lesions showed extensive necrotizing tissue debris, histocytes/lymphocytes reaction, micro-calcification and no viable tumor tissue (Fig. 2d). In the 15-day post-IRE treatment animals (Group 3), 5 out of 6 treated lesions showed no remnant viable tumor but giant cell reaction, hemosiderin-ladden histocyte reaction and scaring fibrosis (Fig. 2e). One out of these 6 treated lesions contained a volume of <5% viable tumor tissue, compared to 68±8% viable tumor tissue for the end point control animals (Group 2) with 32 ±8% central necrosis due to tumor ischemia. Histologically determined tumor viability characteristics (percentage of viable tumor tissue estimated for each lesion at necropsy) for all animals in Groups 1, 2 and 3 are shown in Fig. 4C.

MR Imaging

T2-weighted, T1-weighted, and proton-density weighted turbo spin echo (TSE) images for baseline control (Group 1) 1.3cm diameter N1-S1 rat hepatoma are shown in Fig. 3. These tumor masses were consistently hyper-intense within T2-wieghted images, hypo-intense within T1-wieghted images and typically iso-intensity within proton-density weighted images.

MRI images demonstrated significant tumor size reductions post-IRE (−32±31%, D_{max} decrease) for treated rats (Group 3) whereas all untreated tumors (Group 2) increased in size (+110±35%, D_{max} increase) (Fig. 4D (left)). Similarly, corresponding two-dimensional C_{max} measurements also demonstrated significant decreases (−52±39%) for treated rats (Group 3) whereas all untreated tumors (Group 2) demonstrated increases in these two-dimensional size measurements (+286±125%) (Fig. 4D (right)). There was a statistically significant difference between both one-dimensional (D_{max}) and two-dimensional (C_{max}) lesion size changes between these two groups ($p = 0.004$ for both comparisons). Representative T2-weighted baseline and follow-up MRI images from a control rat and a 15-day post-IRE treatment rat are shown in Figs. 4A and 4B, respectively. Corresponding H&E histology slides for these rats showed mostly viable tumor tissue for the end point control rat, but no remnant viable tumor in the treated animal.

Immunohistochemistry

For immunohistochemistry CD34 staining, diffuse sinusoidal CD34 reactivity was observed for untreated rat hepatoma (Fig. 5a) whereas 1-day post-IRE CD34 staining showed mild vascular dilation and congestion (Fig. 5b). Remnant vessel skeletons with inflammatory cell infiltration and fibrotic tissue formation over a necrotic background was observed for 7-day and 15-day post-IRE treatment lesions (Figs. 5c and 5d); limited caspase 3 staining was demonstrated in the untreated tumors (typically within central ischemic areas) while most viable tumor tissues demonstrated no caspase 3 activation (Fig. 6a). Extensive caspase 3 activation was observed one day post-IRE treatment (Fig. 6b). At delayed post-IRE follow-up interval (7–15 days post-IRE), caspase 3 was no longer visible within the treated lesion over the necrotic background (Fig. 6c).

Discussion

These animal model studies demonstrated the potential efficacy of IRE as a targeted ablation technique for the treatment of HCC. MR images showed a significant tumor size reduction within 15 days post-therapy and histology correlation studies showed a clear progression from poorly differentiated viable hepatoma tissue pre-therapy to extensive tumor necrosis and complete tumor regression in 9 out of 10 treated rats 7–15 days after treatment. Our study is the first to demonstrate the efficacy of IRE for targeted treatment of liver tumors in a transplanted rodent hepatoma model.

Relatively early post-IRE therapy (within one day post-treatment), we observed homogeneously necrotizing tissues within treated normal liver parenchyma with clear margins between the treated and untreated tissues. However, we observed somewhat different responses within N1-S1 tumor tissues; specifically, tumor tissues tended to exhibit heterogeneously necrotic characteristics at the early intervals (1–3 days) post-therapy with limited viable tumor trapped within the necrotic tissues. Eventually, all treated tumors progressed from these early interval stages of partial necrosis to essentially complete necrosis with fibrotic scar formations 7–15 days later. One potential explanation for these heterogeneous delays in cell death could be that some of the treated tissues were destroyed due to the alternative mechanisms of ischemia and associated hypoxia (due to entrapment within surrounding necrotic tissue) as opposed to the direct effect of irreversible electroporation. Additional studies will be required to rigorously investigate the mechanism of these observed temporally-dependent necrosis events associated with IRE ablation procedures. For tumor tissues, even though no significant changes were observed on H&E and CD34 staining one-day post-therapy (Group 4), we observed extensive caspase 3 activation which might indicate an alternative underlying cell death mechanism (i.e. tumor cell apoptosis initiation) in addition to solely cell membrane permeablization. Delayed interval results (15 days post-therapy) consistently demonstrated the longitudinal efficacy of

this targeted IRE approach; MRI scans depicted significant lesion size reductions for each treated animal whereas significant tumor growth occurred for untreated animals. These imaging results were well correlated to delayed-interval histopathological results that showed no viable tumor tissue within the lesion along with inflammatory cell reaction, fibrotic scar formation, remnant vascular skeleton CD34 positive staining (depicting system of damaged blood vessel walls within the treated tissue region) and an absence of caspase 3 activation.

Our study specifically demonstrated the feasibility of using IRE as a therapeutic modality for the treatment of HCC. All treated tumors demonstrated significant size reductions within two weeks post-therapy and there were no adverse events (i.e. peritoneal bleeding, tumor seeding, liver failure or mortalities) observed for any of the eighteen treated animals. For the IRE protocol selected for our study, we used far fewer pulses than prior cutaneous tumor model studies (8 square wave pulses as opposed to 80 pulses at 0.3Hz) while continuing to achieve effective treatment response. Our study demonstrated the feasibility of using IRE to ablate HCC, however, further studies to optimize IRE parameters are certainly warranted.

The efficacy of conventional RFA approaches is often limited in larger tumors due to perfusion-mediated cooling which can limit thermally-induced coagulation necrosis (39). The extent of the treated tissue volume can be difficult to control due to blood circulation with heat-sink effects leading to indistinct margins between treated and untreated tissues and/or under-treatment of the targeted tissues ((40)). IRE results in a distinct margin between ablated and viable tissues at the position where the magnitude of the electrical field falls below a lethal dose threshold (23). Importantly, IRE does not suffer from the ‘heat-sink’ effect that is commonly problematic for thermal ablation methods (21). Additional potential advantages for IRE methods include tumor specific immunological reaction (41), little impact upon the collagen network within treated tissues and the potential to abate tumor tissues near large vessels (42). Finally, application of the electroporation pulses during IRE procedures requires <1s. This feature contrasts significantly with the time duration required for RFA methods that typically involve application of thermal energy for upwards of 8–20min/ablation to achieve sufficient temperatures for coagulative necrosis (43). Recently, a commercially developed electroporation device received 510k approval from the FDA (NanoKnife™, AngioDynamics Inc.). Given the promising results of our current IRE ablation studies in the N1-S1 rat hepatoma model, future studies are warranted to further investigate the efficacy of such devices for targeted treatment of liver tumors as well as additional tumor etiologies that can be difficult to treat with conventional ablation methods.

One limitation of our study was the lack of intra-procedural imaging guidance to optimize the placement of IRE electrodes; sub-optimal electrode placement could conceivably have led to the incomplete response observed for one rat in Group 3. During previous studies, ultrasound (US) imaging methods were used for intra-procedural visualization of IRE ablation procedures (44). In future HCC IRE studies, US, MRI, or CT techniques could be used to optimize placement of IRE electrodes to ensure that the targeted tumor mass is entirely contained within the anticipated IRE ablation zone. Functional imaging methods (dynamic contrast-enhanced CT/MRI and/or diffusion-weighted MRI) may prove useful for immediate or early detection of IRE treatment response.

For these initial studies we did not individually tailor the IRE protocol (voltage, electrode spacing) to produce an ablation zone specific to each individual tumor size. We simply used a single IRE protocol producing an ablation zone size that we anticipated would be sufficiently large to cover all tumors below one given size. For our studies, we did not experience any gross complications due to damage to adjacent liver parenchyma. However, we would anticipate that the use of much larger ablation zones would lead to decomposition and subsequent liver failure. An individualized, patient-specific approach could be important for clinical IRE applications

given a desire to spare normal liver tissues to preserve function. As demonstrated during prior studies ((30)), optimization of the IRE ablation volumes should be possible using pre-procedural FEM simulations. Further studies are warranted to rigorously investigate the potential to individually tailor the size of IRE ablation zones to ensure complete treatment of targeted tumors while sparing as much surrounding normal liver tissue as possible.

In conclusion, this pre-clinical study demonstrated the feasibility of using irreversible electroporation as a novel ablation modality for targeted treatment of hepatoma in the N1-S1 rat model. Follow-up MRI images demonstrated significant tumor size reductions and histology correlation studies demonstrated extensive tumor necrosis within 7–15 days post-therapy. IRE is a promising new approach for liver-directed treatment of HCC and may offer multiple potential benefits over conventional ablation methods.

Abbreviations

IRE	Irreversible electroporation
HCC	Hepatocellular carcinoma
AASLD	American Association for the Study of Liver Diseases
PEI	percutaneous ethanol injection
PAI	percutaneous acetic acid injection
RFA	radiofrequency ablation
MCT	microwave coagulation therapy
MRI	magnetic resonance imaging
T2W TSE	T2-weighted turbo spin echo
TR/TE	repetition and echo time
H&E staining	hematoxylin and eosin staining

Acknowledgments

Financial Support:

This publication was made possible by Grant Number CA134719 from the National Cancer Institute and also Grant Number UL1 RR025741 from the National Center for Research Resources (NCRR), both components of the National Institutes of Health (NIH), and NIH Roadmap for Medical Research. Its contents are solely the responsibility of the authors and do not necessarily represent the official view of NCRR or NIH.

References

1. Parkin DM, Bray F, Ferlay J, Pisani P. Global cancer statistics, 2002. CA Cancer J Clin 2005;55:74–108. [PubMed: 15761078]
2. Llovet JM, Bruix J. Novel advancements in the management of hepatocellular carcinoma in 2008. J Hepatol 2008;(48 Suppl 1):S20–S37. [PubMed: 18304676]
3. Llovet JM, Burroughs A, Bruix J. Hepatocellular carcinoma. Lancet 2003;362:1907–1917. [PubMed: 14667750]
4. Callstrom MR, Charboneau JW. Technologies for ablation of hepatocellular carcinoma. Gastroenterology 2008;134:1831–1835. [PubMed: 18486619]
5. Bruix J, Sherman M. Management of hepatocellular carcinoma. Hepatology 2005;42:1208–1236. [PubMed: 16250051]
6. Livraghi T. Percutaneous ethanol injection in the treatment of hepatocellular carcinoma in cirrhosis. Hepatogastroenterology 2001;48:20–24. [PubMed: 11268965]

7. Tsai WL, Cheng JS, Lai KH, et al. Clinical trial: percutaneous acetic acid injection vs. percutaneous ethanol injection for small hepatocellular carcinoma--a long-term follow-up study. Aliment Pharmacol Ther 2008;28:304–311. [PubMed: 19086330]
8. Lencioni R, Cioni D, Crocetti L, et al. Early-stage hepatocellular carcinoma in patients with cirrhosis: long-term results of percutaneous image-guided radiofrequency ablation. Radiology 2005;234:961–967. [PubMed: 15665226]
9. Lau WY, Lai EC. The current role of radiofrequency ablation in the management of hepatocellular carcinoma: a systematic review. Ann Surg 2009;249:20–25. [PubMed: 19106671]
10. Liang P, Dong B, Yu X, et al. Prognostic factors for survival in patients with hepatocellular carcinoma after percutaneous microwave ablation. Radiology 2005;235:299–307. [PubMed: 15731369]
11. Vogl TJ, Muller PK, Hammerstingl R, et al. Malignant liver tumors treated with MR imaging-guided laser-induced thermotherapy: technique and prospective results. Radiology 1995;196:257–265. [PubMed: 7540310]
12. Hinshaw JL, Lee FT Jr. Cryoablation for liver cancer. Tech Vasc Interv Radiol 2007;10:47–57. [PubMed: 17980318]
13. Vilana R, Bruix J, Bru C, Ayuso C, Sole M, Rodes J. Tumor size determines the efficacy of percutaneous ethanol injection for the treatment of small hepatocellular carcinoma. Hepatology 1992;16:353–357. [PubMed: 1322349]
14. Livraghi T, Giorgio A, Marin G, et al. Hepatocellular carcinoma and cirrhosis in 746 patients: long-term results of percutaneous ethanol injection. Radiology 1995;197:101–108. [PubMed: 7568806]
15. Cho YK, Kim JK, Kim MY, Rhim H, Han JK. Systematic review of randomized trials for hepatocellular carcinoma treated with percutaneous ablation therapies. Hepatology 2009;49:453–459. [PubMed: 19065676]
16. Tateishi R, Shiina S, Teratani T, et al. Percutaneous radiofrequency ablation for hepatocellular carcinoma. An analysis of 1000 cases. Cancer 2005;103:1201–1209. [PubMed: 15690326]
17. Harrison LE, Koneru B, Baramipour P, et al. Locoregional recurrences are frequent after radiofrequency ablation for hepatocellular carcinoma. J Am Coll Surg 2003;197:759–764. [PubMed: 14585410]
18. Rhim H. Complications of radiofrequency ablation in hepatocellular carcinoma. Abdom Imaging 2005;30:409–418. [PubMed: 15688113]
19. Teratani T, Yoshida H, Shiina S, et al. Radiofrequency ablation for hepatocellular carcinoma in so-called high-risk locations. Hepatology 2006;43:1101–1108. [PubMed: 16628706]
20. Davalos RV, Mir IL, Rubinsky B. Tissue ablation with irreversible electroporation. Ann Biomed Eng 2005;33:223–231. [PubMed: 15771276]
21. Onik G, Mikus P, Rubinsky B. Irreversible electroporation: implications for prostate ablation. Technol Cancer Res Treat 2007;6:295–300. [PubMed: 17668936]
22. Al-Sakere B, Andre F, Bernat C, et al. Tumor ablation with irreversible electroporation. PLoS ONE 2007;2:e1135. [PubMed: 17989772]
23. Edd JF, Horowitz L, Davalos RV, Mir LM, Rubinsky B. In vivo results of a new focal tissue ablation technique: irreversible electroporation. IEEE Trans Biomed Eng 2006;53:1409–1415. [PubMed: 16830945]
24. Miller L, Leor J, Rubinsky B. Cancer cells ablation with irreversible electroporation. Technol Cancer Res Treat 2005;4:699–705. [PubMed: 16292891]
25. Lee EW, Loh CT, Kee ST. Imaging guided percutaneous irreversible electroporation: ultrasound and immunohistological correlation. Technol Cancer Res Treat 2007;6:287–294. [PubMed: 17668935]
26. Rubinsky J, Onik G, Mikus P, Rubinsky B. Optimal parameters for the destruction of prostate cancer using irreversible electroporation. J Urol 2008;180:2668–2674. [PubMed: 18951581]
27. Davalos RV, Rubinsky B. Temperature considerations during irreversible electroporation. International journal of heat and mass transfer 2008;51:5617–5622.
28. Novikoff AB. A transplantable rat liver tumor induced by 4-dimethylaminoazobenzene. Cancer Res 1957;17:1010–1027. [PubMed: 13489702]

29. Miklavcic D, Semrov D, Mekid H, Mir LM. A validated model of in vivo electric field distribution in tissues for electrochemotherapy and for DNA electrotransfer for gene therapy. Biochim Biophys Acta 2000;1523:73–83. [PubMed: 11099860]
30. Edd JF, Davalos RV. Mathematical modeling of irreversible electroporation for treatment planning. Technol Cancer Res Treat 2007;6:275–286. [PubMed: 17668934]
31. Ju S, McLennan G, Bennett SL, et al. Technical aspects of imaging and transfemoral arterial treatment of N1-S1 tumors in rats: an appropriate model to test the biology and therapeutic response to transarterial treatments of liver cancers. J Vasc Interv Radiol 2009;20:410–414. [PubMed: 19167243]
32. Therasse P, Arbuck SG, Eisenhauer EA, et al. New guidelines to evaluate the response to treatment in solid tumors. European Organization for Research and Treatment of Cancer, National Cancer Institute of the United States, National Cancer Institute of Canada. J Natl Cancer Inst 2000;92:205–216. [PubMed: 10655437]
33. World Health Organization. WHO Handbook for Reporting Results of Cancer Treatment. Switzerland: Geneva; 1979.
34. Varma M, Jasani B. Diagnostic utility of immunohistochemistry in morphologically difficult prostate cancer: review of current literature. Histopathology 2005;47:1–16. [PubMed: 15982318]
35. Fox SB, Harris AL. Histological quantitation of tumour angiogenesis. Apmis 2004;112:413–430. [PubMed: 15563306]
36. Yagi T, Hardin JA, Valenzuela YM, Miyoshi H, Gores GJ, Nyberg SL. Caspase inhibition reduces apoptotic death of cryopreserved porcine hepatocytes. Hepatology 2001;33:1432–1440. [PubMed: 11391532]
37. Najimi M, Smets F, Sokal E. Hepatocyte apoptosis. Methods Mol Biol 2009;481:59–74. [PubMed: 19096793]
38. Garin E, Denizot B, Roux J, et al. Description and technical pitfalls of a hepatoma model and of intra-arterial injection of radiolabelled lipiodol in the rat. Lab Anim 2005;39:314–320. [PubMed: 16004691]
39. Ahmed M, Lobo SM, Weinstein J, et al. Improved coagulation with saline solution pretreatment during radiofrequency tumor ablation in a canine model. J Vasc Interv Radiol 2002;13:717–724. [PubMed: 12119331]
40. Goldberg SN, Hahn PF, Halpern EF, Fogle RM, Gazelle GS. Radio-frequency tissue ablation: effect of pharmacologic modulation of blood flow on coagulation diameter. Radiology 1998;209:761–767. [PubMed: 9844671]
41. Al-Sakere B, Bernat C, Andre F, et al. A study of the immunological response to tumor ablation with irreversible electroporation. Technol Cancer Res Treat 2007;6:301–306. [PubMed: 17668937]
42. Maor E, Ivorra A, Leor J, Rubinsky B. The effect of irreversible electroporation on blood vessels. Technol Cancer Res Treat 2007;6:307–312. [PubMed: 17668938]
43. Dodd GD 3rd, Soulen MC, Kane RA, et al. Minimally invasive treatment of malignant hepatic tumors: at the threshold of a major breakthrough. Radiographics 2000;20:9–27. [PubMed: 10682768]
44. Rubinsky B, Onik G, Mikus P. Irreversible electroporation: a new ablation modality--clinical implications. Technol Cancer Res Treat 2007;6:37–48. [PubMed: 17241099]

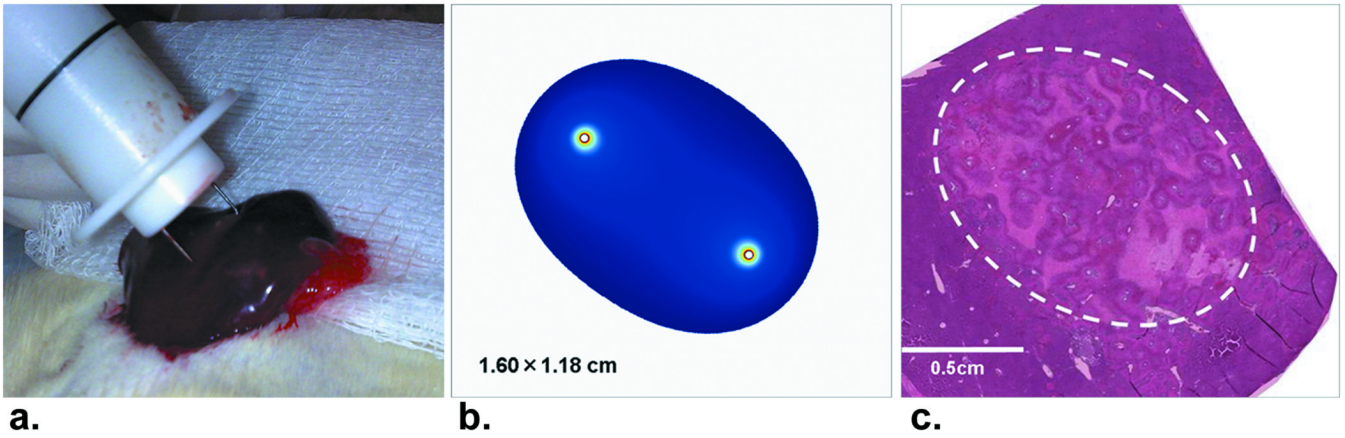

Figure 1.

(**a**) Photograph showing the IRE electrode placement within the targeted hepatic lobe. (**b**) Finite element modeling simulation of the anticipated IRE ablation zone with the selected IRE parameters. (**c**) H&E staining showing an ablation region of coagulative necrosis and a well delineated margin between treated and untreated liver tissues for Sprague-Dawley rat euthanized 24 hours post-IRE procedure (×25).

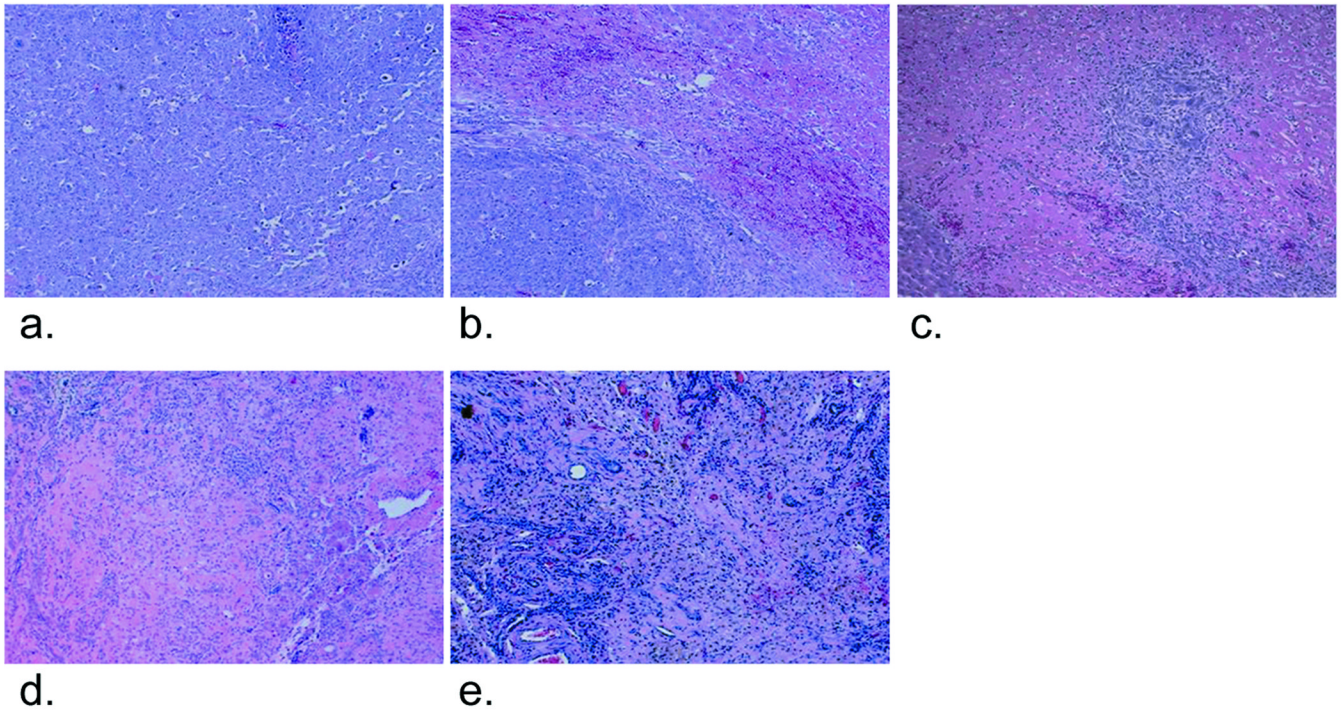

Figure 2.

H&E staining of N1-S1 rat HCC at increasing intervals post-therapy (×200). (**a**) Untreated HCC, showing viable tumor. (**b**) 1-day post-therapy, showing that most of the tumor remains viable while adjacent liver tissue is necrotizing. (**c**) 3-day post-therapy showed heterogeneously necrotizing tumor and liver tissue. (**d**) 7-day post-therapy, showed extensive necrotizing tissue debris, histocytes/lymphocytes reaction, micro-calcification and no viable tumor. (**e**) 15-day post-therapy, showing no viable tumor but giant cell reaction, hemosiderin-ladden histocyte reaction and scaring fibrosis.

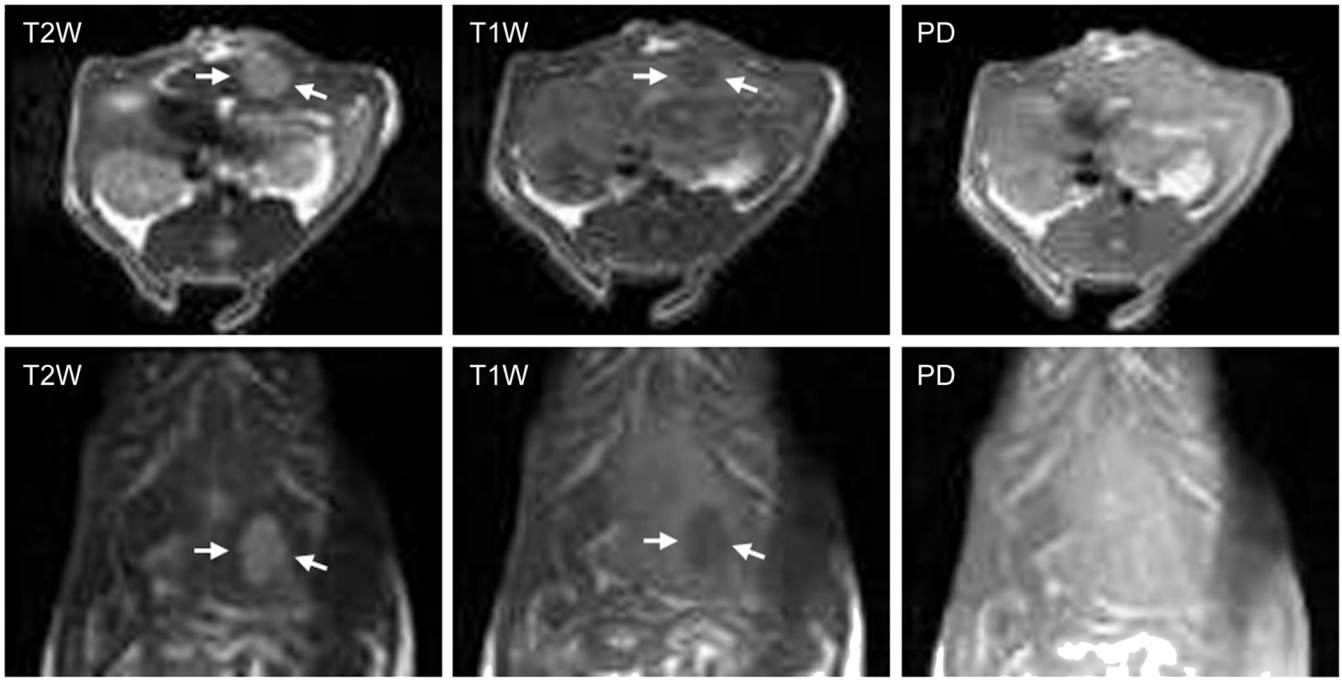

Figure 3.
Representative axial (top row) and coronal (bottom row) T2-weighted (T2W), T1-weighted (T1W), and proton-density (PD) weighted turbo spin echo (TSE) images for a 1.5cm diameter N1-S1 HCC during a baseline control scan (Group 1). N1-S1 HCC were hyper-intense within T2-wieghted images, hypo-intense within T1-wieghted images and typically iso-intense (relative to adjacent normal liver parenchyma) within proton-density weighted images. Arrows within images indicate tumor position.

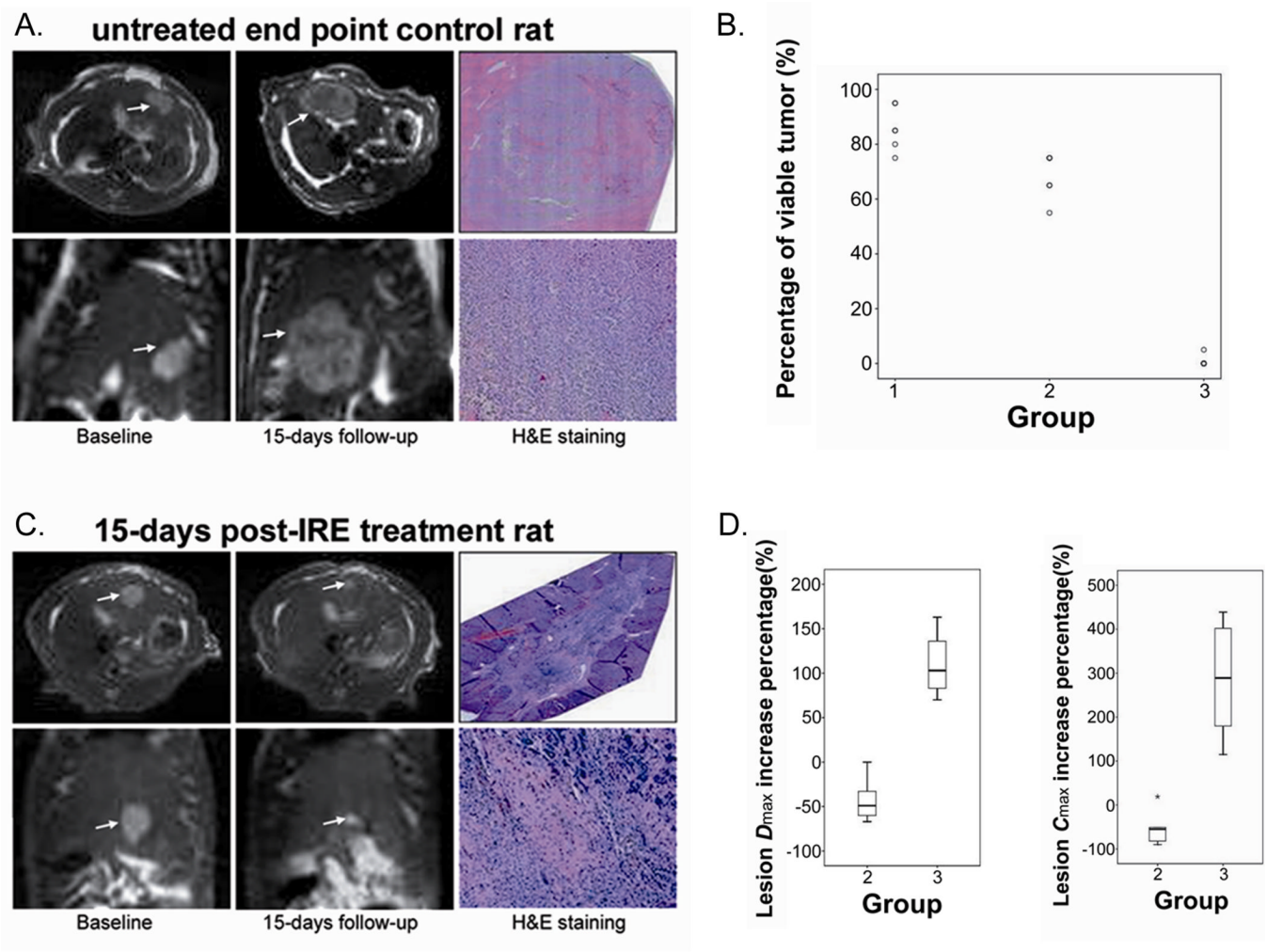

Figure 4.

Axial and coronal orientation MRI images along with corresponding pathological H&E slide images for an untreated 15-day endpoint control rat (**A**) and a 15-day post-IRE treatment rat (**B**). Notice the significant increase in tumor size for the untreated rat (**A**) compared to the notable tumor size reduction for the IRE treated animal (**B**) (arrows indicate tumor positions). H&E pathology slides showed 70% viable tissue within untreated tumor (**A**) and whereas completed tumor regression within the IRE treated rat (**B**). Scatter plot (**C**) shows the pathology-confirmed percentage of viable tumor tissue for 6 rats at baseline control interval (Group 1), 6 untreated control rats following 15-day growth period after original baseline scan (Group 2), and 6 IRE-treated rats following the same 15-day growth period (Group 3). Box plots (**D**) show the lesion D_{max} increase (left) and C_{max} increase (right) for 15-day follow-up animals in untreated control Group 2 and IRE-treated Group 3. The boundary of the boxes closest to zero indicates 25th percentile, line within boxes shows median and boundary of boxes furthest from zero indicates 75th percentile. Outliers are represented as stars. D_{max} and C_{max} increases for Group 2 rats were significantly greater than D_{max} and C_{max} increases for Group 3 rats (p=0.004 for both comparisons using non-parametric Mann-Whitney U-test).

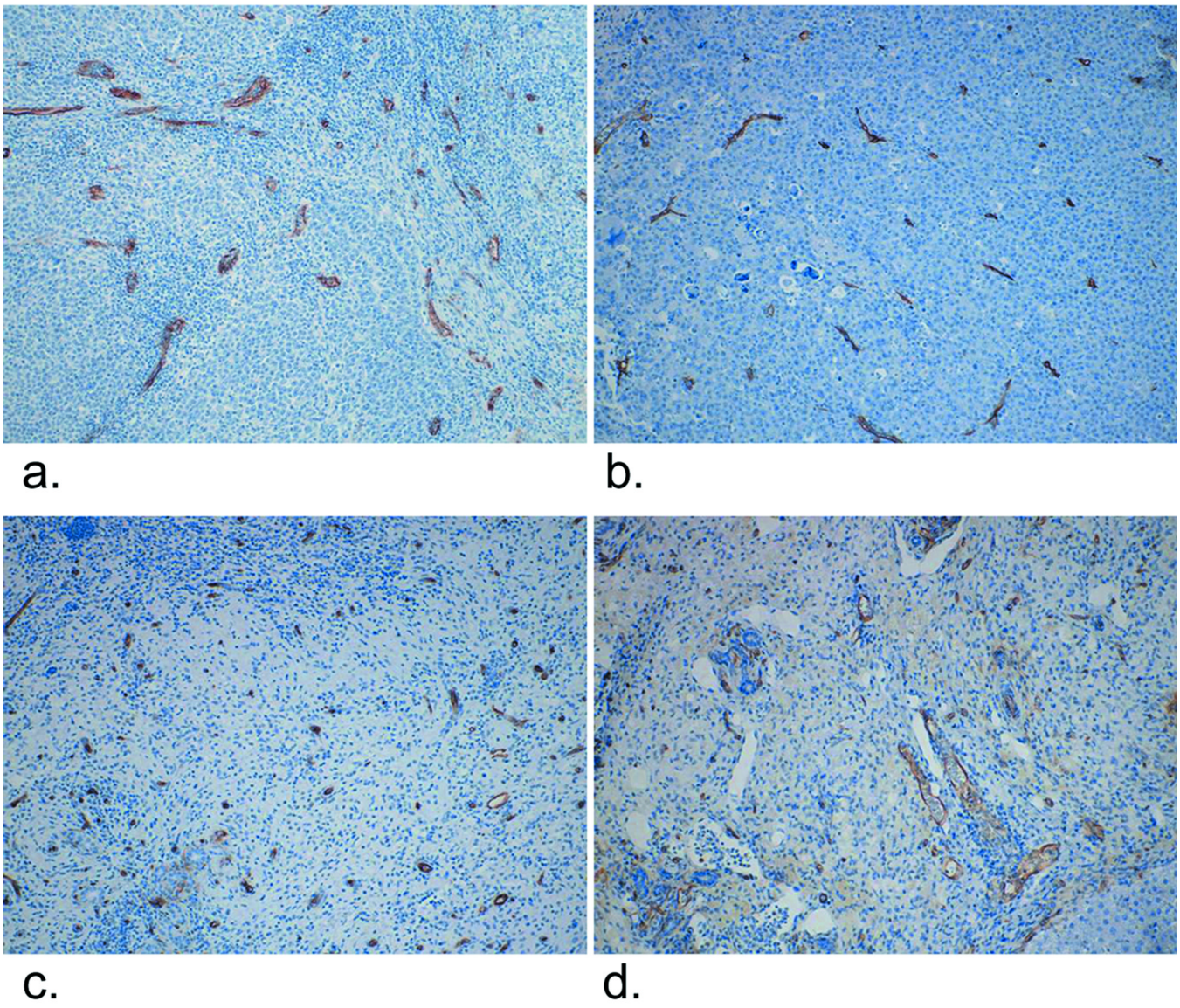

Figure 5.
CD 34 staining (×200). (**a**) Untreated N1-S1 rat HCC showing diffuse sinusoidal CD34 reactivity, (**b**) 1-day post-IRE treatment showed mild vascular dilation and congestion, (**c**) 7-day and (**d**) 15-day post-IRE therapy, showing remnant vessel skeletons with inflammatory cell infiltration and fibrotic tissue formation over a necrotic background.

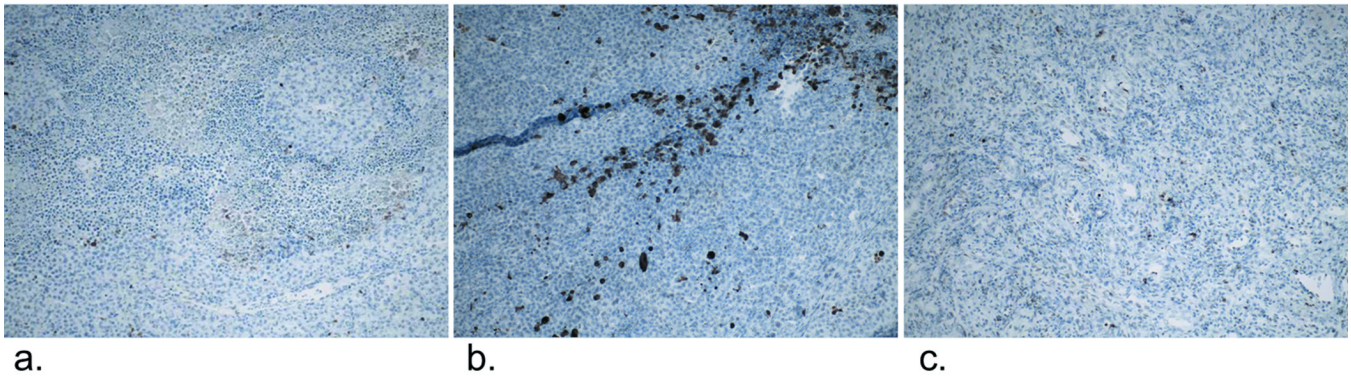

Figure 6.
Caspase 3 staining (×200). (**a**) untreated N1-S1 rat HCC. (**b**) 1-day post-IRE treatment, showing extensive activation of caspase 3. (**c**) 7-day post-IRE treatment, caspase 3 activation was no longer visible over a necrotic background across the entire lesion.